Heterogeneous Catalysis

DOI: 10.1002/anie.201206505

Tailored Mesostructured Copper/Ceria Catalysts with Enhanced Performance for Preferential Oxidation of CO at Low Temperature**

Hoang Yen, Yongbeom Seo, Serge Kaliaguine, and Freddy Kleitz**

Hydrogen as the most efficient and cleanest energy source for fuel cell power is produced mainly by reformation of hydrocarbons, followed by the water gas shift reaction. The CO (0.5–2%) present in the hydrogen stream must be selectively removed because CO is highly poisonous to the electrocatalyst in proton-exchange membrane fuel cells (PEMFCs). Preferential oxidation (PROX) of CO in excess H_2 is therefore a key reaction for the practical use of H_2 in PEMFCs.[1,2]

Among the catalysts reported to be active for PROX, copper/ceria-based catalysts have been considered as promising candidates because of their low cost and high selectivity compared to catalysts based on gold or platinum. However, they usually only show noticeable activities above 100°C, while the operating temperature of PEMFCs is around 80°C.[2a–c,3a,b] Furthermore, the catalytic properties depend strongly on the preparation method and the CuO/CeO_2 interfacial area.[2a–c,3] Despite numerous studies about PROX catalysts, little is known concerning the influence of pore size and pore structure on the catalytic performance.[2a] Transition-metal oxides exhibiting mesoporous structures, for example, Co_3O_4 and CuO/Fe_2O_3, are active for CO oxidation at low temperature and show higher activity than the corresponding bulk materials.[2c–f] The high activity of mesoporous metal oxides was correlated to their ordered mesostructure and high surface area.[2c–f] Hard templating is a method known to enable the synthesis of materials that possess a highly defined pore architecture and a very high surface area, thus leading to unique physicochemical properties.[4] However, studies of surface redox reactivity and the confinement of reactions near to the surface owing to the dimension of the pores have been limited to a few compositions of catalysts for CO oxidation.[2d–f]

Herein, we report the catalytic performance in CO-PROX of Cu/CeO_2 and CuM/CeO_2 catalysts prepared by the nanocasting method.[5a] In this study, mesoporous catalysts with various compositions were synthesized using an improved hard templating method that we have recently developed. The pore size, specific surface area, and pore structure were tailored by changing the type of mesoporous silica used as solid template (e.g., KIT-6 aged at different temperatures, SBA-15, and MCM-48 nanospheres). The resulting metal oxide materials possess a high surface area (up to 200 $m^2 g^{-1}$) and a pore size ranging from 3 nm to 12 nm. The catalytic performance of these materials is among the best reported thus far for copper/ceria-based catalysts with respect to the CO conversion and CO_2 selectivity at low temperature. The effect of their mesostructure and composition on the reducibility and catalytic properties are also substantiated.

Mesoporous silica templates with different pore structures (KIT-6, SBA-15, and MCM-48) were synthesized according to the literature.[5b–d] The pore size of the KIT-6 was varied by changing the aging temperature (40, 100, and 130°C).[5b,c] The nanocast catalysts were prepared by one-step-impregnation hard templating (see Experimental Section). The samples prepared from KIT-6 were labeled as Cu(x)CeM(y)-K-T, with T representing the aging temperature of KIT-6, x ($x = 10$–30) and y ($y = 20$) are nominal molar percentages of Cu or M to Ce (M = Co or Fe), respectively. The samples using SBA-15 and MCM-48 hard templates were denoted as Cu(x)Ce-SBA and Cu(x)Ce-MCM, respectively. Representative TEM images of the nanocast materials replicated from KIT-6 and SBA-15 templates confirm the long-range periodic order of the mesopores (Figure 1 A and B, and Figure S1 in the Supporting Information). The TEM image of Cu/CeO_2 replicated from MCM-48 spheres clearly show the mesoporous spherical particle morphology. Mesoporosity was further confirmed by N_2 adsorption–desorption measurements (Figure S2). All of the samples casted from SBA-15, as well as from KIT-6 aged at 100 and 130°C, showed type IV isotherms with a capillary condensation step above $p/p_o = 0.4$, which are rather typical for mesoporous metal oxide nanocasts.[2d–f,4d]

Narrow pore size distributions were observed for all the samples except for Cu/CeO_2 produced from KIT-6-40. Pore-size analysis, obtained from the adsorption branch by NLDFT methods (see characterization section in the Supporting Information), indicated mesopores of approximately 5 nm

[*] H. Yen, Prof. F. Kleitz
Department of Chemistry and Centre de Recherche sur les Matériaux Avancés (CERMA), Université Laval
Quebec, G1V 0A6 (Canada)
E-mail: freddy.kleitz@chm.ulaval.ca
S. Kaliaguine
Department of Chemical Engineering, Université Laval
Quebec G1V 0A6 (Canada)
E-mail: Serge.Kaliaguine@gch.ulaval.ca
Y. Seo
Department of Chemistry
Graduate School of Nanoscience and Technology (WCU)
KAIST, Daejeon (Republic of Korea)

[**] This work was supported by NSERC (Canada) and FQRNT (Province of Quebec). Y.S. acknowledges support from the National Research Foundation (National Honor Scientist Program 20110031411) and the World Class University Program (R312011000100710) in Korea. The authors thank Prof. Ryong Ryoo (KAIST, Korea) for access to a high-resolution TEM microscope, Jean-François Rioux (Université Laval, Canada) for the Raman spectroscopy data, and Stephane Turgeon and Dr. Pascale Chevallier (Biotechnology and Bioengineering Unit, CHUQ, Quebec, Canada) for kindly supplying XPS data.

Supporting information for this article is available on the WWW under http://dx.doi.org/10.1002/anie.201206505.

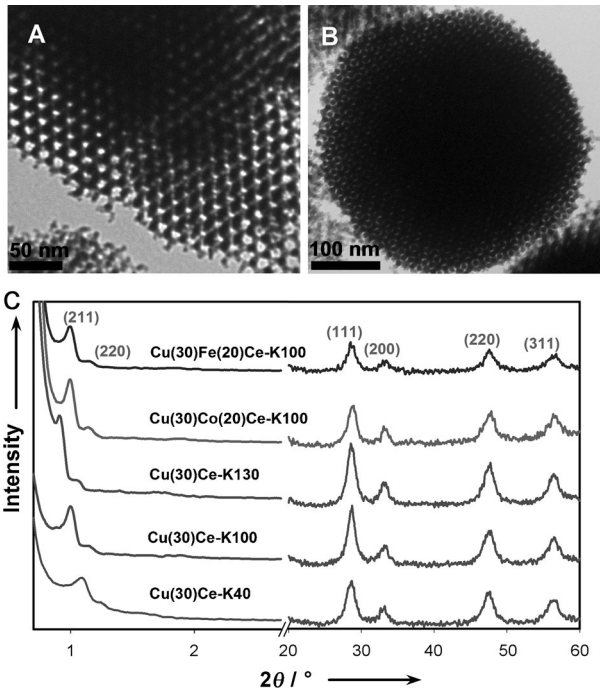

Figure 1. TEM images of A) Cu(30)Ce-K40 and B) Cu(30)Fe(20)Ce-K100. C) Powder XRD patterns of the samples templated from KIT-6.

for the products prepared from SBA-15, KIT-6-100, and KIT-6-130; the sample replicated from MCM-48 showed a smaller pore size of 2.6 nm. On the other hand, Cu(30)Ce-K40 exhibited additional pore-size distributions at about 12 nm and 16 nm, which is rather similar to what is observed when metal oxides could grow randomly within one set of the pore system of the bicontinuous structure, possibly owing to low interconnectivity between the two subnetworks of mesopore channels in the parent KIT-6 silica aged at low temperature.[2f,4d–g] Textural parameters of the mesoporous metal oxide samples are given in Table S1.

Specific BET surface area, pore size, and pore volume of the nanocast Cu(30)Ce-K samples all decrease with higher aging temperature of the KIT-6 silica template. The samples prepared from cubic (*Ia3d*) KIT-6-100 and 2D hexagonal (*p6mm*) SBA-15 have the same pore size ($\approx$5 nm), specific surface area ($\approx 150\ m^2 g^{-1}$), and pore volume ($\approx 0.3\ cm^3 g^{-1}$). In contrast, Cu(30)Ce-K40 and Cu(30)Ce-MCM have a noticeably higher surface area ($\approx 200\ m^2 g^{-1}$), however the former has larger pore size and higher pore volume. Note that variation in copper content and additional incorporation of Co or Fe dopants have a minor effect on surface area and pore volume of the nanocast products. However, such differences in composition also have a significant impact on the reducibility and catalytic properties for CO-PROX (see below).

The excellent mesostructure order of the mesoporous metal oxides was also demonstrated by low-angle XRD patterns (Figure 1C and Figure S3). All the patterns exhibit a main strong peak at low 2θ value, which could be indexed to the (211) and (100) reflections of the *Ia3d* and *p6mm* symmetries, respectively. The d values calculated from the (211) reflection of the cubic mesophase are 8.11, 8.84, and 9.71 nm, corresponding to unit-cell parameters (a_o) of 19.9, 21.7, and 23.8 nm for the mesoporous Cu(30)Ce samples derived from KIT-6 aged at 40, 100, and 130 °C, respectively. The crystalline nature of the walls of the mesoporous materials was confirmed by wide-angle PXRD analysis (Figure 1C and Figure S4), which reveals peaks corresponding to the pure face-centered-cubic (*fcc*) structure of CeO_2. The absence of other oxide phases of copper, cobalt, or iron suggests that these metal species are highly dispersed or incorporated in the ceria lattice. The quantification of bulk and surface composition was carried out by AAS and XPS (Table S2). The remaining Si content determined by AAS is about 3.5 wt % in all samples. It is likely that ceria-bound Si species could not be totally removed in the presence of Si–O–Ce bonds (isolated SiO_2 is readily dissolved with NaOH), which is consistent with other reports on the preparation of CeO_2 using silica template.[6a] Surface Cu/Ce ratios in the samples were 2.1–2.8 times higher than the respective Cu/Ce ratios in the bulk. This result confirms the surface enrichment with Cu and its high dispersion, in agreement with the elemental EDX mapping (Figure S5) and XRD results. From the XPS spectra (Figure S6), it is apparent that most Cu present in these samples is in +1 oxidation state, owing to the presence of low Cu $2p_{3/2}$ binding energy (932 eV) and the absence of shake-up peaks that are characteristics of Cu^{2+} at 939–944 eV.[3b–c] Cerium species in all of the samples seem to be mostly in a +4 oxidation state. These observations are indicative of a redox equilibrium ($Cu^{1+} + Ce^{4+} \leftrightarrow Cu^{2+} + Ce^{3+}$), which has been claimed to be the source of a synergetic effect on catalyst reducibility.[3] These results prove that the copper species are well dispersed and in close contact with ceria. Temperature-programmed reduction by H_2 (H2-TPR) of pure CeO_2 and metal-doped CeO_2 samples were performed to investigate reducibility characteristics of the catalysts (Figure 2). Two broad peaks appear at about 582 and 781 °C for pure CeO_2, belonging to the reduction of surface and bulk ceria, respectively.[6b] Bulk CuO shows a single reduction peak at 320 °C. For Cu(*x*)Ce-K100 materials, hydrogen consumption can roughly be divided in two reductive peaks (denoted as α and β), which can be attributed to the reduction of well-dispersed surface copper species and copper in the ceria lattice, respectively, at noticeably lower temperature com-

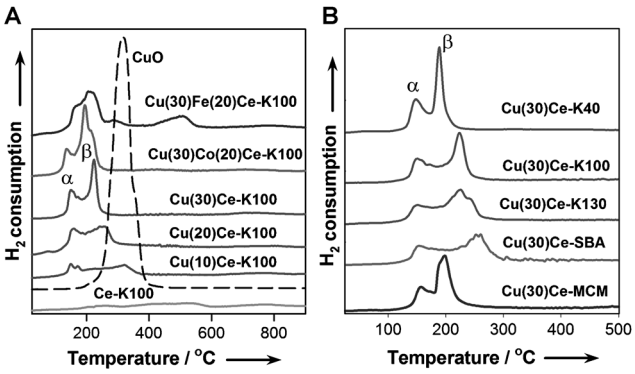

Figure 2. H_2-TPR profiles of the compositions replicated from A) KIT-6-100 and B) Cu(30)Ce from different mesoporous silica templates.

pared to the bulk oxide.[3,6] With an increase of the Cu content from 10 to 30%, the temperature of the α peak decreases slightly and the associated H_2 consumption increases from 0.21 to 0.5 mmol per gram of catalyst, reflecting higher amount of the most reducible Cu species on the surface. The β peak position drops strongly from 321 to 223 °C, and the total H_2 consumption below 400 °C increases from 0.78 to 1.65 mmol g^{-1} with increasing Cu content. Note that the total H_2 consumption always surpasses the amount needed to totally reduce $Cu^{+/2+}$ species into Cu^0, which implies that some of Ce^{4+} ions are also reduced at lower temperature along with reduction of $Cu^{+/2+}$. Indeed, the H_2-TPR results demonstrate that there is a strong synergistic interaction between copper and cerium species that facilitates reduction of both copper and cerium. Doping of Co or Fe into the copper/ceria structure leads to higher H_2 consumption (Table S3), and an additional peak appears at 489 °C in the case of the Fe incorporation. Moreover, Figure 2 B shows the H_2-TPR profiles of the Cu(30)Ce materials nanocast from different mesoporous silica templates. These samples have similar content and segregation of Cu species. The Cu(30)Ce-MCM has the smallest pore size (≈2.6 nm), but higher H_2 uptake for the α peak compared to those of the Cu(30)Ce-K130 and Cu(30)Ce-SBA samples, which have a larger pore size (≈4.9 nm), probably because of the higher surface area of the Cu(30)Ce-MCM sample. For Cu(30)Ce-K samples, the total H_2 consumption below 400 °C and the temperatures of the α peaks are the same, while the β peak shifts to lower temperature with decreased aging temperature of the KIT-6 templates. Notably, the H_2 uptake at the α peaks is 0.36, 0.52, and 0.94 for the samples prepared from KIT-6 templates aged at 130, 100, and 40 °C, respectively, thus suggesting that the catalysts become more reducible with lower aging temperature of the parent silica template. Thus, these results evidence that both the composition and textural parameters of the catalysts have pronounced effects on their reducibilities. In addition, contributions of other effects, such as differences in Cu dispersion in CeO_2 originating from variation in silanol densities in the silica hard templates, which could play a role in the process of nanocasting (templates aged at varying temperatures), cannot be excluded. Oxygen vacancies are believed to play an important role in CO oxidation and can be considered as an indicator for promotion of the reaction.[3b–c] Direct evidence of oxygen vacancies and defects can be provided by Raman spectroscopy, as they cause changes in the vibrational structure of the ceria lattice. As shown in Figure 3 and Figure S7, for pure CeO_2, a broad band with high intensity at 462 cm^{-1} is assigned to the F2g vibration mode of the CeO_2 lattice. The bands at 580 and 1160 cm^{-1} can be ascribed to the presence of oxygen vacancies and defects in the CeO_2 lattice.[7] The Raman spectra of copper/ceria samples exhibit an increase in intensity of the band at 1160 cm^{-1}, while the F2g vibration band shifts from 462 to 446 cm^{-1}, becoming broader and partially overlapping with the band at 580 cm^{-1}. The reason for these features could be the presence of oxygen vacancies, which are related to structural defects generated by incorporation of heterovalent atoms.[7] These observations made by Raman spectroscopy agree well with the above conclusions

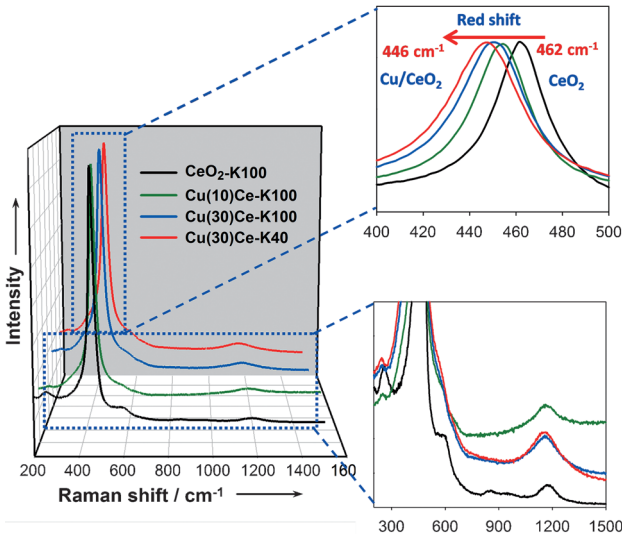

Figure 3. Raman spectra of the nanocast mixed oxide samples with various compositions and structures.

concerning reducibility and correlation with the textural characteristic of the catalysts. The increase in copper content, surface area, and pore size leads to higher number of oxygen vacancies and increased reducibility. Here, oxides with 3D cubic pore structure seem to exhibit more oxygen vacancies and higher reducibility than the analog with 2D hexagonal pore structure. This result could tentatively be correlated to the continuous pore structure of the cubic mesophase possibly associated to subtle variations in wall thickness of the different replicas.

The corresponding activity and selectivity for CO-PROX of all the samples, plotted as function of temperature, are given in Figure 4 and Figure S8. The light-off temperature of CO (T50) decreases in the following order for copper/ceria catalysts: Cu(10)Ce-K100 > Cu(20)Ce-K100 > Cu(30)Ce-K130 > Cu(30)Ce-SBA > Cu(30)Ce-MCM > Cu(30)Ce-K100 > Cu(30)Ce-K40, in accordance with the evolutions in oxygen vacancies and reducibility. Especially, a complete CO conversion with 100% selectivity was achieved at around 40 °C in the case of Cu(30)Ce-K40, which is thus among the most active copper/ceria catalysts reported to date. Considering the low temperature, this material might also be exploited for practical application in gas sensors or breathing-protection masks. Furthermore, the incorporation of 20% Fe extends the full CO conversion (80–160 °C) and improves selectivity to CO_2, while Co incorporation does not provide substantial improvement. Further studies will be necessary to clarify the origin of the impact of the Fe and Co doping. Note that the stability of the catalyst was verified for the example of Cu(30)Ce-K100, and only a slight deterioration of the catalytic performance was found after three cycles.

In summary, we have shown that highly active and selective mesoporous copper/ceria catalysts with tailored compositions and textural parameters can be obtained through nanocasting using mesoporous silica phases as hard templates. The products are promising materials for application as CO-PROX catalysts or as gas sensors. In addition to

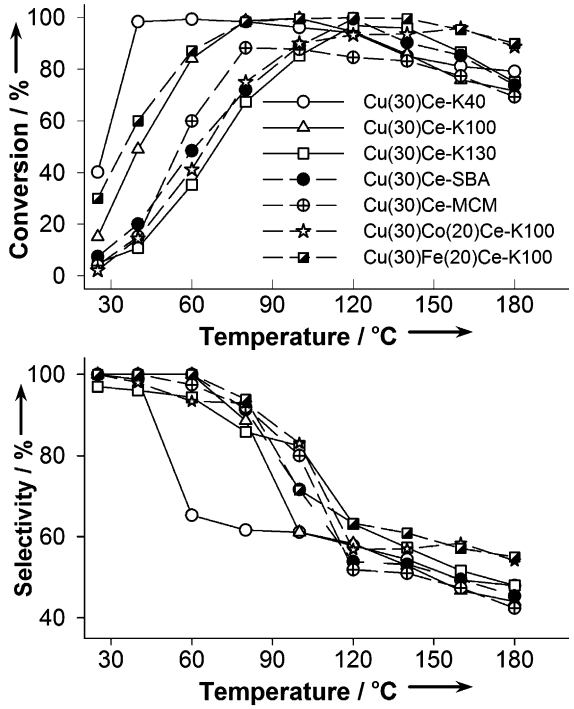

Figure 4. Conversion and selectivity as a function of temperature for CO-PROX over the nanocast catalysts (1.64% CO, 1.62% O_2, 90.25% H_2, balance He, space velocity: 37 $l h^{-1} g^{-1}$).

the role of composition and specific surface area, the reducibility and catalytic performance are also influenced by structural parameters such as pore size and pore structure. This study demonstrates that a fine control over nanoscale structural features offers new perspectives for catalyst design.

Experimental Section

For the preparation of the nanocast metal oxides, preground nitrate salts (2.75 g) in desired proportions ($Cu(NO_3)_2{\cdot}3H_2O$, $Ce(NO_3)_3{\cdot}6H_2O$, $Co(NO_3)_2{\cdot}6H_2O$, $Fe(NO_3)_3{\cdot}9H_2O$) were mixed and ground with the silica template (1 g, pretreated in vacuum at 150 °C for 2 h) in an agate mortar in the presence of *n*-hexane (10 mL). Metal precursors (1.5 g) were used in the case of KIT-6[5b,c] aged at 40 °C as the template. The resulting homogeneous mixture was subsequently dispersed in *n*-hexane (30 mL) and heated to reflux (80 °C) for 20 h. After filtration, the samples were dried at 70 °C for 24 h, and calcined under air at 500 °C for 5 h. The silica template was then removed by treatment with 2 M NaOH (three times for 24 h) at room temperature. Finally, the resulting Cu/CeO_2 or CuM/CeO_2 powders were washed three times with water and three times with ethanol, and then dried at 70 °C.

Received: August 13, 2012
Published online: October 22, 2012

Keywords: carbon monoxide · fuel cells · mesoporous materials · metal oxides · oxidation

[1] a) R. Farrauto, S. Hwang, L. Shore, W. Ruettinger, J. Lampert, T. Giroux, Y. Liu, O. Ilinich, *Annu. Rev. Mater. Res.* **2003**, *33*, 1 – 27; b) S. Alayoglu, A. U. Nilekar, M. Mavrikakis, B. Eichhorn, *Nat. Mater.* **2008**, *7*, 333 – 338; c) Q. Fu, W.-X. Li, Y. Yao, H. Liu, H.-Y. Su, D. Ma, X.-K. Gu, L. Chen, Z. Wang, H. Zhang, B. Wang, X. Bao, *Science* **2010**, *328*, 1141 – 1144; d) A. U. Nilekar, S. Alayoglu, B. Eichhorn, M. Mavrikakis, *J. Am. Chem. Soc.* **2010**, *132*, 7418 – 7428.

[2] a) Y. Zhang, H. Liang, X. Y. Gao, Y. Liu, *Catal. Commun.* **2009**, *10*, 1432 – 1436; b) E. D. Park, D. Lee, H. C. Lee, *Catal. Today* **2009**, *139*, 280 – 290; c) J.-L. Cao, Y. Wang, X.-L. Yu, S.-R. Wang, S.-H. Wu, Z.-Y. Yuan, *Appl. Catal. B* **2008**, *79*, 26 – 34; d) Y. Ren, Z. Ma, L. Qian, S. Dai, H. He, P. G. Bruce, *Catal. Lett.* **2009**, *131*, 146 – 154; e) M. Jin, J.-N. Park, J. K. Shon, J. H. Kim, Z. Li, Y.-K. Park, J. M. Kim, *Catal. Today* **2012**, *185*, 183 – 190; f) H. Tüyüz, M. Comotti, F. Schüth, *Chem. Commun.* **2008**, 4022 – 4024.

[3] a) G. Avgouropoulos, T. Ioannides, *Appl. Catal. B* **2006**, *67*, 1 – 11; b) C. S. Polster, H. Nair, C. D. Baertsch, *J. Catal.* **2009**, *266*, 308 – 319; c) R. Kydd, W. Y. Teoh, K. Wong, Y. Wang, J. Scott, Q.-H. Zeng, A.-B. Yu, J. Zou, R. Amal, *Adv. Funct. Mater.* **2009**, *19*, 369 – 377.

[4] a) X. Ji, J. K. T. Lee, L. F. Nazar, *Nat. Mater.* **2009**, *8*, 500 – 506; b) P. G. Bruce, B. Scrosati, J.-M. Tarascon, *Angew. Chem.* **2008**, *120*, 2972 – 2989; *Angew. Chem. Int. Ed.* **2008**, *47*, 2930 – 2946; c) C. Y. Ma, Z. Mu, J. J. Li, Y. G. Jin, J. Cheng, G. Q. Lu, Z. P. Hao, S. Z. Qiao, *J. Am. Chem. Soc.* **2010**, *132*, 2608 – 2613; d) H. Tüysüz, E. L. Salabaş, E. Bill, H. Bongard, B. Spliethoff, C. W. Lehmann, F. Schüth, *Chem. Mater.* **2012**, *24*, 2493 – 2500; e) H. Tüysüz, C. W. Lehmann, H. Bongard, B. Tesche, R. Schmidt, F. Schüth, *J. Am. Chem. Soc.* **2008**, *130*, 11510 – 11517; f) Y. Doi, A. Takai, Y. Sakamoto, O. Terasaki, Y. Yamauchi, K. Kuroda, *Chem. Commun.* **2010**, *46*, 6365 – 6367; g) F. Jiao, A. H. Hill, A. Harrison, A. Berko, A. V. Chadwick, P. G. Bruce, *J. Am. Chem. Soc.* **2008**, *130*, 5262 – 5266.

[5] a) H. Yen, Y. Seo, R. Guillet-Nicolas, S. Kaliaguine, F. Kleitz, *Chem. Commun.* **2011**, *47*, 10473 – 10475; b) F. Kleitz, F. Bérubé, R. Guillet-Nicolas, C. M. Yang, M. Thommes, *J. Phys. Chem. C* **2010**, *114*, 9344 – 9355; c) F. Kleitz, S. H. Choi, R. Ryoo, *Chem. Commun.* **2003**, 2136 – 2137; d) T.-W. Kim, P.-W. Chung, V. S.-Y. Lin, *Chem. Mater.* **2010**, *22*, 5093 – 5104.

[6] a) N. C. Strandwitz, G. D. Stucky, *Chem. Mater.* **2009**, *21*, 4577 – 4582; b) F. Giordano, A. Trovarelli, C. Leitenburg, M. Giona, *J. Catal.* **2000**, *193*, 273 – 282; c) P. Bera, K. R. Priolkar, P. R. Sarode, M. S. Hegde, S. Emura, R. Kumashiro, N. P. Lalla, *Chem. Mater.* **2002**, *14*, 3591 – 3601.

[7] a) J. R. McBride, K. C. Hass, B. D. Poindexter, W. H. Weber, *J. Appl. Phys.* **1994**, *76*, 2435 – 2441; b) J. E. Spanier, R. D. Robinson, F. Zhang, S.-W. Chan, I. P. Herman, *Phys. Rev. B* **2001**, *64*, 245407.

